Monthly Notices
of the
ROYAL ASTRONOMICAL SOCIETY

Mon. Not. R. Astron. Soc. **403,** 714–730 (2010) doi:10.1111/j.1365-2966.2009.16181.x

Dynamical models for the formation of elephant trunks in H II regions

Jonathan Mackey★ and Andrew J. Lim★†

Dublin Institute for Advanced Studies, 31 Fitzwilliam Place, Dublin 2, Ireland

Accepted 2009 December 7. Received 2009 November 30; in original form 2009 September 25

ABSTRACT

The formation of pillars of dense gas at the boundaries of H II regions is investigated with hydrodynamical numerical simulations including ionizing radiation from a point source. We show that shadowing of ionizing radiation by an inhomogeneous density field is capable of forming so-called *elephant trunks* (pillars of dense gas as in e.g. M16) without the assistance of self-gravity or of ionization front and cooling instabilities. A large simulation of a density field containing randomly generated clumps of gas is shown to naturally generate elephant trunks with certain clump configurations. These configurations are simulated in isolation and analysed in detail to show the formation mechanism and determine possible observational signatures. Pillars formed by the shadowing mechanism are shown to have rather different velocity profiles depending on the initial gas configuration, but asymmetries mean that the profiles also vary significantly with perspective, limiting their ability to discriminate between formation scenarios. Neutral and molecular gas cooling are shown to have a strong effect on these results.

Key words: hydrodynamics – radiative transfer – methods: numerical – H II regions.

1 INTRODUCTION

Among the most striking features of H II regions are the long columns of neutral gas pointing towards the central star, known variously as elephant trunks (ETs), pillars and fingers. The most famous examples are the 'pillars of creation' in the Eagle Nebula (M16), observed with the *Hubble Space Telescope* (*HST)* by Hester et al. (1996). The *HST* images of NGC 3372 (the Carina Nebula) clearly show a number of ETs as do *HST* images of NGC 3603 (Brandner et al. 2000). The Elephant Trunk Nebula in IC 1396, observed by e.g. Reach et al. (2004), is another typical example. Carlqvist, Gahm & Kristen (2003) show ETs in the Rosette Nebula (NGC 2237-2246), IC 1805 and N81.

The M16 pillars have been well studied observationally. They are towards the more massive end of the scale of observed ETs but are not extreme, so we have used their properties as a benchmark for our simulation results. Hester et al. (1996) studied the surface of the M16 pillars in detail with *HST*, finding that the interface between the pillars and the H II region is well explained by a thin ionization front (I-front) with a strong photoevaporation flow into the lower density ionized gas. Due to the large opacity of the molecular gas, they could say little about the interior of the pillars. Molecular CO maps were obtained by Pound (1998), who showed that the pillars are mostly molecular, that the internal and external pressures are comparable and that their photoevaporation times are about 2×10^7 yr. He also found strong velocity gradients in the molecular emission, but it is not clear if this indicates a coherent flow generated by pillar formation. White et al. (1999), using infrared, millimetre and radio observations, found the pillars to have cold cores ($\sim$20 K), with surrounding warm ($\simeq$60 K) gas and an outer 'hot' shell (at $\sim$250–320 K). The clumps at the heads of the pillars appeared to have typical densities of 2×10^5 cm^{-3}, while the trunks exhibited lower mean densities of 3–5 $\times$ 10^4 cm^{-3}. These authors also found that the internal pressure of the heads of the pillars is a factor of $\sim$2 lower than the adjacent ionized gas pressure. They interpreted this as evidence that the heads of the pillars are in the early stages of radiatively driven implosion (Bertoldi 1989), and may therefore be $<$100 kyr old. Subsequent dynamical models by Williams, Ward-Thompson & Whitworth (2001) suggest alternate scenarios in which the pillars could be 200–400 kyr old.

Despite detailed observations, and a long history of theoretical models, there is as yet no clear consensus as to how such features as ETs arise, their lifetimes or their end states. It has been suggested that instabilities in I-fronts can generate similar structures or, alternatively, that pre-existing inhomogeneities in the interstellar medium (ISM) will create shadowed regions behind dense clumps where gas can accumulate. The question of which of these scenarios actually forms ETs was discussed at least as far back as Kahn (1958). Given that the ISM is clumpy, and that instabilities are present under certain conditions, it is likely that both processes contribute to some degree. Thus the difficulty from a theoretical perspective is that there are a number of potentially viable mechanisms to form pillars, and it is difficult to observationally distinguish between them. The instability model was proposed by Frieman (1954) for Rayleigh–Taylor instabilities and subsequently developed for

★E-mail: jmackey@cp.dias.ie (JM); Andrew.Lim@csr.com (AJM)
†Present address: Cambridge Silicon Radio Ltd., Churchill House, Cambridge Business Park, Cowley Road, Cambridge CB4 OWZ.

I-front instabilities. These instabilities have been studied by many authors but are not the subject of this paper, so we refer the reader to recent work by e.g. Williams (2002), Mizuta et al. (2006) and Whalen & Norman (2008, and references therein). We concentrate here on modelling the effects of the shadowing of dense clumps on the dynamics of an expanding I-front. Lim & Mellema (2003) found that a partially shadowed clump in an ionizing radiation field was pushed further into the shadowed region, and a denser and longer lived tail arose compared to that of a single isolated clump. This was in the context of Earth-mass clumps in planetary nebulae (O'Dell & Handron 1996) which have lifetimes of a few thousand years. For more massive clumps, the longer lifetimes may allow much denser tails to develop in the shadowed regions, possibly to the extent that they would be observed as pillars. This was also suggested by Pound et al. (2007).

General models of the evolution of a photoevaporating clump and the shadowed region behind it were developed by Bertoldi & McKee (1990) and Lefloch & Lazareff (1994), although these were mostly concerned with the dense clump itself. Williams et al. (2001) used computational models to study formation scenarios of the M16 pillars, setting up axisymmetric simulations with various initial density fields exposed to planar ionizing radiation. They found that with their modelling assumptions, multiple initial scenarios were capable of producing dense structures resembling the ETs seen in M16. These were found to be long-lived quasi-equilibrium structures, raising the possibility that the pillars could be quite old ($\gtrsim$300 kyr). Their work highlights the difficulty in interpreting the observations – a number of different initial conditions and physical processes could produce pillars. More recently, Miao et al. (2006) used a smoothed particle hydrodynamics code with radiative transfer to model the photoionization of a dense cloud; their results supported the idea that the head of the pillar is in the early stages of radiation-driven implosion. Their modelling was of the head more than the trunk, however, and it remains unclear whether a pillar could form behind the imploding head on a time-scale as short as 100 kyr. Pound et al. (2007) modelled the photoionization of a single dense clump ($M = 30\,\mathrm{M}_{\odot}$) by an O star, specifically looking at the shadowed region. They found that the shadow can produce a long neutral tail of the dimensions of the M16 pillars, but without enough material in the tail. They note that adding in multiple clumps of different sizes should increase the amount of tail material, as was found by Lim & Mellema (2003), a suggestion we explore in detail in this paper.

The first global simulation of the expansion of an H II region into a turbulent density field was presented by Mellema et al. (2006a). They found that features such as ETs developed quite naturally due to the uneven I-front expansion velocity, but due to the nature of the simulation individual pillars are poorly resolved. Mac Low et al. (2007) also modelled global expansion of an H II region, but their simulations were more of the early I-front expansion than of the later dynamical evolution. Very recently, Gritschneder et al. (2009) modelled part of an expanding H II region with planar radiation impinging on a turbulent density field. They also found that pillar-like features developed naturally in their simulations after about 250 kyr, but again the resolution in individual pillars is poor. Lora, Raga & Esquivel (2009) also follow a similar approach to form pillar-like structures. They study the angular momentum of dense clumps which form in their simulation and find preferential alignment perpendicular to the direction of the radiation field. In work that is in some ways similar to ours, but on much smaller scales, Raga et al. (2009) showed how photoevaporation flows from a large reservoir of dense gas can flow into shadowed regions, recombine, cool and begin to build up dense pillar-like structures.

With some exceptions (Williams et al. 2001; Pound et al. 2007; Raga et al. 2009), these works were not primarily focused on how ETs form, and as a result it is difficult to tell which physical processes are most relevant. The aim of this work is to focus on the shadowing mechanism to see how effectively it can produce ETs in an idealized environment. We have developed a radiation-magnetohydrodynamics (MHD) code with which to study this problem. We will describe our code and algorithms in Section 2. In Section 3, we describe the initial conditions and show results from 3D simulations of the photoionization of a density field with randomly distributed dense clumps. These models show a number of structures resembling ETs which form dynamically due to shadowing in the inhomogeneous medium. In Section 4, we simulate certain clump configurations in isolation to demonstrate two different ways pillars could form. The first model has the clumps oriented almost like a pillar in the initial conditions, whereas in the second model clumps are swept past each other into a pillar-like structure. We find that neutral gas cooling has a strong effect on our results and in Section 5 we repeat these two models using an alternate thermal model with moderately strong neutral gas cooling. The details and evolutionary time-scales change considerably, but the formation mechanisms remain unchanged. In Section 6 we discuss the context and significance of our results, and in Section 7 we present our conclusions.

2 NUMERICAL METHODS AND ALGORITHMS

2.1 Fluid dynamics

We have written a modular, finite volume, fluid dynamics code to run these simulations. The code uses a uniform grid in one, two or three spatial dimensions with cubic cells. Scalar and vector fields are both cell-centred. The integrator for the fluid equations is based on the algorithm described by Falle, Komissarov & Joarder (1998), which is dimensionally unsplit and second-order accurate in time and space. We have separate Riemann solvers for the Euler and ideal MHD equations. We also add some artificial viscosity in a similar manner to Falle et al. (1998) using a coefficient of $\eta_v = 0.05$–0.1. This is required to ensure that shocks travel at the correct speed in all directions. It fixes e.g. the 'carbuncle problem' in the double Mach reflection test [Woodward & Colella (1984) used the Lapidus viscosity prescription for this] and mitigates the Quirk instability (Quirk 1994) for stationary grid-aligned shocks.

2.2 Ray-tracing and microphysics

Our ray-tracing and microphysics routines are based largely on the methods in Lim & Mellema (2003) and on the C^2-ray method developed by Mellema et al. (2006b). We use operator splitting to first update the dynamics by a full time-step and then run the microphysics update over the full time-step. In this work, we only consider explicitly the ionization of atomic hydrogen. We first describe the ray-tracing algorithm and then the microphysics calculation.

The short characteristics tracer (e.g. Raga et al. 1999) is used to trace out rays from a source in a causal manner, calculating the optical depth to a cell by interpolating between (previously calculated) optical depths to neighbouring cells closer to the source. Given that we are ignoring diffuse radiation (the on-the-spot approximation), the diffusion in the ray tracer is not significant and is minimized using the weighting scheme given by Mellema et al. (2006b).

When the photoionization time is short compared to other time-scales (cooling, recombination and collisional ionization times) the

microphysics equations become difficult to solve explicitly, so we adopt a dual approach. In cases of weak photoionization, we use an explicit fifth-order Runge–Kutta technique with adaptive step-size to a given relative accuracy (Press et al. 1992). For strong photoionization we integrate explicitly until the hydrogen ion fraction, x, satisfies $x \geq 0.95$, and then analytically integrate the equations assuming a constant electron density (as described in Mellema et al. 2006b), with bisection substepping to convergence (typically two to four substeps). For both of these methods, we use a relative error tolerance of 0.001.

This algorithm also calculates the time-averaged optical depth through the cell $\Delta\tau$, which is then used by subsequent cells in the ray tracer. Mellema et al. (2006b) use a simple time average of $\Delta\tau$; however, we use a time average of $\exp(-\Delta\tau)$ since this gives a time average of the fraction of photons passing through the cell. This can be easily seen in the (extreme) case of an optically thick cell which is photoionized 'rapidly' half-way through a unit time-step, so that

$$\Delta\tau(t) = \left\{ \begin{array}{cc} 100 & t < 0.5 \\ 0 & 0.5 < t < 1 \end{array} \right\}. \quad (1)$$

The mean optical depth over the time-step is 50, but clearly half of the incident photons will pass through the cell, and $\int_0^1 \exp(-\Delta\tau)\,\mathrm{d}t = 0.5$ gives the desired result. We do this integration at the same time as the microphysics variables, to the same accuracy criterion.

We use monochromatic radiation with a hydrogen photoionization cross-section of $6.3 \times 10^{-18}\,\mathrm{cm}^2$ and an energy gain of 5.0 eV per photoionization. Collisional ionization rates are calculated with fitting functions from Voronov (1997), and radiative recombination (case B) rates using the tables calculated by Hummer (1994). The difference between planar radiation and radiation from a point source can be quite significant if the size of the computational domain is comparable to the distance to the source. The rocket effect is weaker further from a point source due to the inverse square law, which may extend the lifetime of any structures that form. This effect can, however, reduce the length of such structures since the intensity of the radiation is higher at their heads. In the case of M16, the heads of the pillars are about 2 pc from the brightest star and they are about 1 pc long, so the flux dilution is more than a factor of 2 along their length. We therefore use a point source in this work.

2.3 Gas cooling

We use two cooling models in this work, denoted C1 and C2, which differ in that C2 has significant cooling in the neutral gas. Our first model, C1, contains four elements as follows.

(i) Radiative losses due to recombining hydrogen, calculated from the non-equilibrium ion fraction and temperature in each cell according to rates tabulated in Hummer (1994).

(ii) Collisional ionization of hydrogen: this is relatively unimportant because the rates are typically very low, but we subtract the ionization energy from the gas for each collisional ionization.

(iii) Cooling due to heavy elements at high temperatures, using the collisional ionization equilibrium (CIE) cooling curve tabulated in Sutherland & Dopita (1993) and shown in their fig. 18. This provides strong cooling in ionized gas with temperatures significantly larger than 10 000 K. Note that in CIE at 10 000 K, hydrogen, nitrogen and oxygen are neutral so this fitting function does not double count the other terms in our cooling function, at least for the gas temperatures encountered in our simulations.

(iv) A linear fit to collisionally excited emission from photoionized oxygen and nitrogen (Osterbrock 1989).

The last term is the most important for this work, since these ionic species are the dominant coolants in H II regions and set the equilibrium temperature in ionized gas of $T_{\rm eq} \simeq 8000$ K. In experiments with different cooling functions for ionized gas, we found that the most important factor for the dynamical evolution of our models was the equilibrium temperature. If the normalization of the cooling function is kept fixed at 8000 K, its slope has little effect on the resulting dynamics so long as the slope is positive. If we had strong shocks in the ionized gas this aspect of the cooling function would have more influence, but the photoionized gas in our simulations has a very narrow temperature range.

In this prescription the neutral atomic gas has no efficient cooling avenue, and shocked neutral gas is typically at 100–10 000 K. This is undoubtedly a limitation in our modelling, but we do not yet model the formation of molecules or the formation/destruction of dust, which are the primary neutral gas coolants in star-forming regions. To assess the effects of significant neutral gas cooling we also use an alternate cooling function, C2, consisting of the previous components in C1 plus additional exponential cooling (Newton's law) in neutral gas with a rate given by

$$\dot{T} = \left[\frac{(1-x)^2}{10^N\ \mathrm{yr}} \right] (T_\infty - T), \quad (2)$$

where T is the gas temperature, T_∞ is the temperature to which this cooling law relaxes at late times, x is the ionization fraction of the gas and N is a parameter specifying the chosen cooling time-scale, $t_c = 10^N\ \mathrm{yr}/(1-x)^2$. The scaling with $(1-x)^2$ ensures that only mostly neutral gas is affected. We set $T_\infty = 100$ K and $N = 4$ for the alternate models run in this paper. This is not an extreme model either in terms of the equilibrium temperature or the cooling time, having less cooling in dense gas than the model presented in Henney et al. (2009). It is a very simple prescription, with an effect which is intermediate between C1 and a two-temperature isothermal model (e.g. Williams et al. 2001; Gritschneder et al. 2009; Lora et al. 2009).

2.4 Code tests

We have extensively tested the fluid dynamics, microphysics and ray-tracing components of the code.[1] For hydrodynamics we used a range of shock-tube tests in 1D (Toro 1999), and then in 2D at various angles to the grid axes, with the code reproducing the correct solutions. We have run the double Mach reflection test (Woodward & Colella 1984) and obtained good agreement with the original work and with e.g. the ATHENA code (fig. 16 in Stone et al. 2008). Since we explicitly add in numerical viscosity, the diffusion is slightly stronger than in the ATHENA code. We have also done tests of implosions and blast waves in 2D and 3D, finding results consistent with previous work (e.g. Stone et al. 2008) and recovering the Sedov–Taylor solution for the adiabatic blast wave in 3D. We have also tested the development of the Kelvin–Helmholz instability (e.g. Agertz et al. 2007), finding very satisfactory agreement with other work.

Raymond (1979) calculated zero-dimensional shock models by following a parcel of gas through a shock front. We have tested our code against his 'Model E', a $100\,\mathrm{km\,s^{-1}}$ steady shock with a 1 μG transverse magnetic field, setting it up in our code as a 1D problem with $100\,\mathrm{km\,s^{-1}}$ gas hitting a dense cold layer and allowing the

[1] A brief description of our code and results from test problems can be found at http://homepages.dias.ie/~jmackey/jmac/.

system to relax to an equilibrium state. Our test reproduced well the ion fractions for hydrogen and helium, the gas temperature and the density as a function of position. We have also run models at higher shock velocity and find that for $v \gtrsim 130\,\mathrm{km\,s^{-1}}$ the shocks become overstable, in agreement with previous work (e.g. Innes, Giddings & Falle 1987).

Photoionization was tested in conjunction with ray tracing using similar tests to those in Mellema et al. (2006b), where the dynamics is switched off. We started with 1D rays from a source at infinity, without dynamics or recombinations. For a grid with 1000 cells, we computed models with cell optical depths $\Delta\tau = \{0.1, 1, 10, 100\}$, and where the total number of time-steps varied from $t_{\rm sim}/\delta t = \{10^1, 10^2, 10^3, 10^4\}$. The error in I-front position compared to the analytic value was found to converge rapidly to less than one cell width with increasing time resolution. For models with recombinations turned on, errors were no more than one cell width for all runs with >10 time-steps per recombination time, except for low-density models where the I-front is resolved.

In 2D and 3D, we computed the expansion of circular and spherical I-fronts from a point source into a static medium, with and without recombinations. Without recombinations, the models provide a test of photon conservation (by comparing the number of ions to photons emitted as a function of time). We plot the photon conservation in the top two panels of Fig. 1, for 2D on the left and 3D on the right. These figures show the relative sizes of ray-tracing and time-integration errors as a function of resolution and dimensionality. For the very low-resolution runs (33^2 and 33^3 cells), we lose between 1 and 10 per cent of photons due to interpolation errors in the ray tracing when the ionized region is <10 cells across. With increased spatial resolution, the errors decrease strongly whereas increased time resolution does not help the 33 cell runs significantly. There is a dramatic improvement in accuracy with time resolution for the 101 and 257 cell runs. These results show that the errors are interpolation dominated when the number of cells is much smaller than the number of time-steps and time integration dominated in the opposite limit. Using the weighting scheme recommended by Mellema et al. (2006b), we find that I-fronts are circular to within a cell width over a wide range of densities, luminosities, and spatial and temporal resolutions.

The lower panels of Fig. 1 show the position of the I-front as a function of time for simulations with recombinations included, modelling the idealized Strömgren sphere analysis and its 2D analogue. The mean I-front position is always within 1–2 per cent of the analytic value except at very early times when it has only crossed a few cells or when the time-steps are of the order of the recombination time, $t_{\rm rec} = (\alpha n_{\rm H})^{-1}$, where α is the (case B) recombination coefficient set to a constant for this test ($\alpha = 2.59 \times 10^{-13}\,\mathrm{cm^3\,s^{-1}}$) and $n_{\rm H}$ is the hydrogen number density. This is an

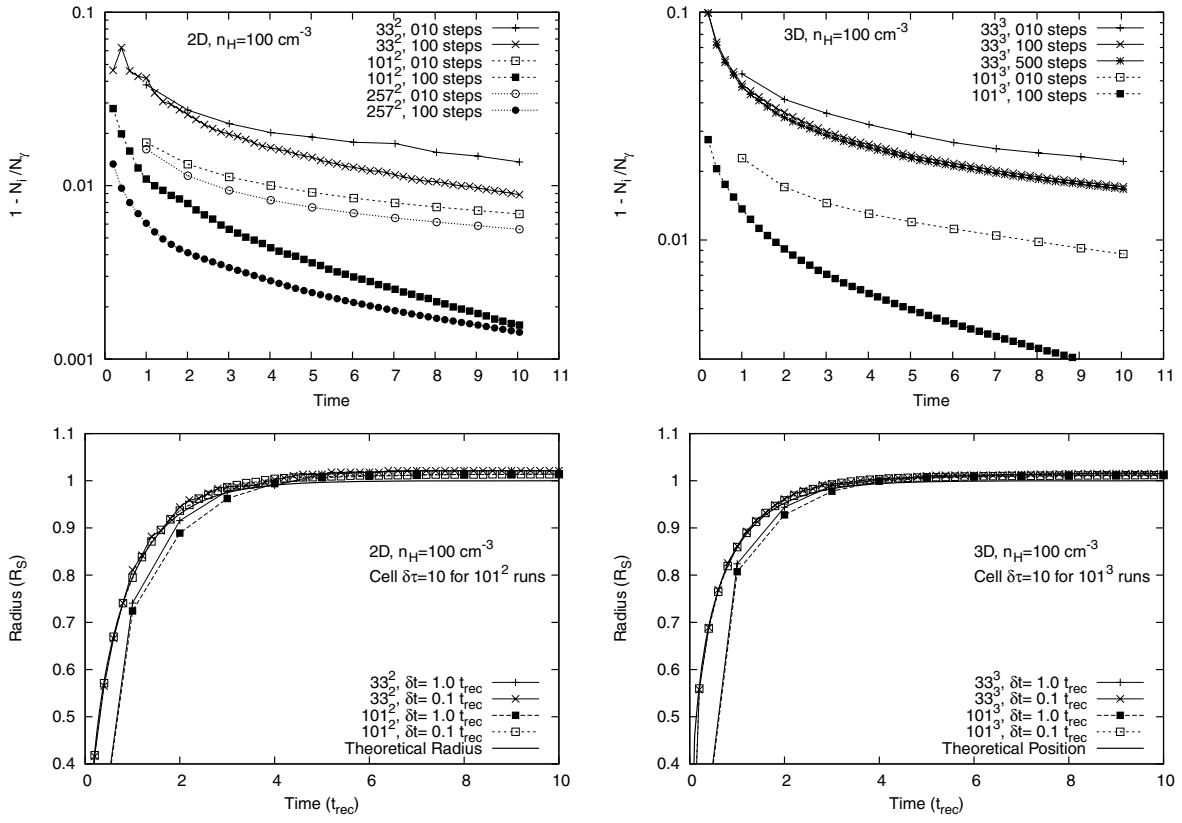

Figure 1. Tests of the radiative transfer algorithm in 2D (left) and 3D (right). The top two plots compare the number of ions to the number of photons emitted for a source in a uniform medium with dynamics and recombinations switched off. The source is at the centre of the domain and the I-front remains on the domain for the duration of the simulations. This is a scale-free problem which we have run with parameters such that the cell optical depth is $\delta\tau = 10$ for the runs with 101^2 and 101^3 cells ($\delta\tau = 30.6$ for lower resolution and 3.93 for higher resolution). We always lose some photons due to the interpolation, but this decreases dramatically with resolution. The lower plots show the evolution of the I-front radius over time for runs with recombinations switched on. Again it is a uniform medium with the same optical depths per cell. The time is shown in units of the recombination time $t_{\rm rec}$ and the radius in units of the Strömgren radius (or its 2D analogue). When the time-step $\delta t = t_{\rm rec}$ the I-front propagates too slowly, but for $\delta t = 0.1 t_{\rm rec}$ it has the correct speed.

expected limitation of the C^2-ray method since it uses time averages of the photon flux through each cell (see Mellema et al. 2006b). For the tests where $\delta t = t_{\rm rec}$, we underestimate the I-front velocity while it expands to the Strömgren radius. The error is slightly larger at higher spatial resolution because we have to do the same inaccurate time average across more cells and the error is always on the side of losing photons. For sufficient time resolution, however, the I-front propagates at the correct speed, and it is worth noting that the photoionization time for a cell is much shorter than the recombination time while the I-front is expanding rapidly. We do not need to resolve this time-scale to get accurate results. This is the major strength of the C^2-ray algorithm.

We have also used our code to reproduce the simulations of Lim & Mellema (2003), where dense clumps in different configurations were photoevaporated by planar ionizing radiation. We find that our code gives largely consistent results despite significant differences in the numerical methods; for example, the Lim & Mellema (2003) simulations did not use an explicitly photon-conserving algorithm.

3 RANDOM CLUMP SIMULATIONS AND RESULTS

Previous studies (e.g. Mellema et al. 2006a; Mac Low et al. 2007; Gritschneder et al. 2009) have used a turbulence model to generate a density field into which the ionizing radiation propagates. In this work, we wish to isolate the shadowing effect of the radiation from other rather uncertain physics such as the type of turbulent motions we inject into the gas. In this respect, our work is more similar to that of Williams et al. (2001). We add dense clumps to a uniform density field in the following way.

(i) We start by setting the mean background density, $n_{\rm b}$, ranging from 10 to 10^3 cm^{-3} in different simulations.

(ii) We choose a total mass to put into clumps by calculating the mass associated with a smoothed mean density in clumpy material, $n_{\rm cl}$, in a subset of the full simulation domain. The subset is chosen to keep clumps away from simulation boundaries, particularly the boundary nearest the radiation source.

(iii) We set the maximum and minimum mass and size of the clumps and draw clumps randomly within these limits until all the mass in clumpy material has been used up. The size of a clump in each direction is chosen separately, so typically we get triaxial clumps.

(iv) The clump's mass and size determine its peak overdensity for a given radial profile. In this work, we use Gaussian profiles.

(v) The clump's position is then set at random on the domain, within the allowed region, and it is rotated by a random angle in all three directions. Clumps are added to the background density field one by one, in a linear superposition when they overlap.

(vi) The initial conditions are static everywhere, and we assign a constant pressure throughout.

The method of random sampling can strongly influence the distribution obtained. Clump positions, radii, orientations and masses are selected randomly within certain minimum and maximum values. In all cases, we select a random number on a linear scale between the two limits.

3.1 2D simulations

The above procedure can also be performed in 2D with slab symmetry, enabling us to do a study with a wider range of parameters than is possible in 3D. We performed 184 2D simulations on a 1.5×1.5 pc^2 domain with a radiation source 2 pc off the domain in one direction. The background densities used were $n_{\rm b} = \{10, 100, 1000\}$ cm^{-3}, the ionizing photon fluxes entering the domain were $F_\gamma = \{10^{10}, 10^{11}, 10^{12}, 10^{13}\}$ cm^{-2} s^{-1} and the number of clumps were $N_{\rm cl} = \{10, 30, 100\}$, being either compact or extended, round or triaxial, with scale radii 0.0225 pc $\leq R_s \leq$ 0.15 pc. Compact round clumps had a radius of 0.05 pc, extended round clumps were 0.12 pc, compact triaxial clumps were [0.0225–0.06] pc and extended triaxial clumps were [0.06–0.15] pc. The total mass in clumps was chosen by the above method, setting a smoothed mean density in clumps of $n_{\rm cl} = \{10^2, 10^3, 10^4\}$ cm^{-3} and calculating the associated mass. For the 2D models, we set the maximum and minimum clump masses to be very close to each other so that all clumps would have similar masses.

In addition to the 184 models with the parameters mentioned above, we also selected particular models and varied the random seeds, also using larger domains to ensure that boundary effects were not important. For models with 10 clumps, the specific clump configuration was important, but for 30 and 100 clumps, the random seed had little effect on whether or not the model produced ETs. The boundary effects were found to be minimal. We use outflow, or zero-gradient, boundary conditions for all of the simulations in this paper. This is the logical choice for the lateral boundaries and for the boundary furthest from the source. For the boundary nearest the source a reflection boundary could be imposed to model a pressure-confined H II region, but we have chosen to model an H II region which has broken out of its parent molecular cloud and is no longer pressure confined in at least some directions.

Care must be taken with the transition from R-type to D-type I-fronts. If this occurs too close to the boundary nearest the source spurious inflows can be set up by rarefaction waves propagating backwards from the stalling I-front. This can introduce an unphysical aspect to the simulation results; therefore, we chose all of our simulation parameters such that the I-front in the background medium remained R-type well into the domain. This ensured that photoevaporation flows dictated the flow at the boundary rather than vice versa. We have verified that the R-type to D-type transition occurs as expected with a shock driven ahead of the I-front into the neutral gas and a strong photoevaporation flow established in the opposite direction.

Of the 184 2D models, approximately 30 produced pillar-like structures, with another $\simeq$20 producing short features more like heaps than pillars and another $\simeq$10 producing very short-lived pillar-like features lasting $<$50 kyr. The most successful groups of models had background and clump densities of $[n_{\rm b}, n_{\rm cl}] = [10^2, 10^3]$ cm^{-3}, $[10^2, 10^4]$ cm^{-3} and $[10^3, 10^4]$ cm^{-3}, with 10 or 30 clumps. Those models which successfully produced pillars had a combination of large low-density regions, where the I-front could propagate far from the source, and large dense clumps, which were capable of stalling the I-front for sufficient time to produce a pillar in the shadowed region. The trunks of the pillars were formed from clump material more than ambient gas, simply because the ambient gas is not dense enough. If the background density was high enough to contribute significantly to a pillar, then it was also high enough to stall the I-front and a pillar could not form. The clump material which made up a pillar always came from several clumps; a lone clump in these models never gathered enough ambient gas into the tail to produce a pillar nor did it contribute enough of its own gas to the shadowed region to form the trunk of a pillar. Typically, pillars formed via the interaction of a number of clumps shadowing each other and accelerating past/through each other produced a dense tail

Table 1. Simulation parameters for the test 3D simulations (1–15) and the one high-resolution model (16). All models have a background density $n_b = 100\,cm^{-3}$ and triaxial clumps as defined in the text, except for models 17 and 18 which have $n_b = 200\,cm^{-3}$ and spherical clumps (see Section 4).

No.	n_{cl}	M_{cl}	N_{cl}	Size	M_J(min/max)	n_{max}	M_J	Flux	Results
1	10^3	72.2	115	C	0.11–1.1	2.7×10^5	12.4	10^{10}	Nothing like ETs; corrugated I-front
2	10^3	72.2	115	C	0.11–1.1	2.7×10^5	12.4	10^{11}	Nothing like ETs; corrugated I-front
3	10^3	72.2	103	E	0.36–1.1	2.0×10^4	45.3	10^{11}	Too diffuse to form dense structures
4	10^3	72.2	40	C	0.36–2.9	9.1×10^5	6.7	10^{10}	Low mass and low-density ETs form
5	10^3	72.2	40	C	0.36–2.9	9.1×10^5	6.7	10^{11}	Short-lived cometary structures
6	10^3	72.2	40	E	1.3–2.6	4.1×10^4	31.7	10^{11}	No dense ET-like structures
7	10^3	72.2	54	C	0.22–2.2	4.8×10^5	9.3	10^{10}	Nothing dense enough or trunk-like
8	10^3	72.2	54	C	0.22–2.2	4.8×10^5	9.3	10^{11}	Nothing dense enough or trunk-like
9	10^3	72.2	85	C	0.14–1.4	4.0×10^5	10.1	10^{10}	Small ET-like structures
10	10^3	72.2	85	C	0.14–1.4	4.0×10^5	10.1	10^{11}	Small cometary structures, low density
11	10^4	666	118	C	1.0–10	3.5×10^6	3.4	10^{11}	Some ETs among large 'mountains'
12	10^4	666	45	C	3.3–27	7.6×10^6	2.3	10^{11}	Multiple dense long-lived ETs
13	10^4	666	40	E	12–24	5.7×10^5	8.5	10^{11}	Large 'mountains' with a few dense ETs
14	10^4	666	59	C	2.0–20	5.1×10^6	2.8	10^{11}	Many dense ETs
15	10^4	666	83	C	1.3–13	3.9×10^6	3.3	10^{11}	Many dense ETs
16	4×10^3	266	40	E	2.4–10.4	1.8×10^5	15.1	10^{11}	Formed long-lived ETs (see Fig. 2)
17	$n_b = 200$	84.9	3	0.1 pc	28.3	1.0×10^5	20.1	2.9×10^{11}	Almost co-linear clumps (see Fig. 3)
18	$n_b = 200$	83.7	3	0.1 pc	27.7–28.3	1.0×10^5	20.1	2.9×10^{11}	Triangular configuration (see Fig. 4)

Note. Clump density, n_{cl}, refers to the mean density of gas put into clumps (cm^{-3}) and the next column M_{cl} gives the total mass in clumps (all masses are in solar masses, $M_\odot$). N_{cl} lists the number of clumps in each model. For size, 'C' refers to compact and 'E' to extended, as described in the text (Section 3.1). M_J(min/max) gives the range of clump masses for the model. The Jeans mass (defined as $M_J = 203\,M_\odot\,T^{1.5}n^{-0.5}$ for adiabatic gas) is calculated for the densest point in the initial conditions (n_{max}) and for a temperature of 10 K. We do not use the actual clump temperatures because the initial constant pressure state has very low temperatures at the densest points ($T \sim 1$ K in some cases); this gives a meaningless Jeans mass since if we included gravity we would not need to impose such an artificially low temperature. The flux is the monochromatic ionizing photon flux ($cm^{-2}\,s^{-1}$) entering the domain. All models use clumps with random positions and properties (within ranges) except models 17 and 18 which are set up to model specific clump configurations in isolation.

which lasted anything from 50 to 200 kyr, depending on the inertia of the leading clump.

3.2 3D test simulations

There are significant differences between the 2D and 3D cases: the stellar flux drops off more rapidly with distance in 3D, shocks in the shadowed regions are converging or diverging whereas in 2D they are planar, and there is also an extra dimension for gas to flow past a clump. These favour the formation of ET-like features in 2D; however, our 2D results can be used to constrain our choice of parameters for more computationally expensive 3D simulations. Some of these differences can be modelled by comparing 2D slab-symmetric and axisymmetric models. For our models, however, it is the asymmetries which generate the ETs and these cannot be modelled in axisymmetry.

Initially we computed 15 3D models with 168×128^2 grid cells, since the 2D models had shown that this was sufficient to resolve the larger features in the simulations. The physical domain was $2.625 \times 2 \times 2\,pc^3$. The parameters we varied in each model are listed in Table 1, models 1–15. All models start with a constant initial pressure of $p_g/k_B = 2 \times 10^5\,cm^{-3}\,K$ where $k_B = 1.38 \times 10^{-16}\,erg\,K^{-1}$ is the Boltzmann constant; this pressure is higher than the typical ISM value and is a compromise between not having the temperature too high in diffuse gas and too low in dense gas. The results are not sensitive to this initial pressure because the ionized gas pressure is 100× greater and it is the pressure difference which drives the dynamical evolution of our models. All 3D models had $n_b = 10^2\,cm^{-3}$; of these, four had $\{n_{cl},\ F_\gamma\} = \{10^3\,cm^{-3}, 10^{10}\,cm^{-2}\,s^{-1}\}$, six used $\{10^3\,cm^{-3}, 10^{11}\,cm^{-2}\,s^{-1}\}$ and five used $\{10^4\,cm^{-3},\ 10^{11}\,cm^{-2}\,s^{-1}\}$. Of these, the models with $n_{cl} = 10^3\,cm^{-3}$ had too little mass in clumps, and none of the models produced anything as dense or massive as a pillar. The models with $n_{cl} = 10^4\,cm^{-3}$, by contrast, did produce massive and long-lived pillars, simply because the initial clumps were so massive and dense. The models with fewer clumps were more successful. With too many clumps there were no large low-density regions, resulting in structures more like mountains than long columns. These dense models were rather unrealistic however, with initial densities in clumps of $n_H \gtrsim 10^6\,cm^{-3}$, very gravitationally unstable, as can be seen by comparing clump masses to Jeans masses in Table 1.

It was difficult to devise an automatic method for identifying candidate ETs in the 3D simulations. Instead we generated images of the volume renderings from a number of viewing angles and picked out structures with $n \geq 10^4\,cm^{-3}$, an aspect ratio of $\gtrsim 2$ and which persisted for >50 kyr. Any candidates were then studied more closely with cross-section and isosurface plots to verify that they could be classified as ETs.

3.3 Large 3D simulation

Based on these tests we tried an intermediate model (model 16 in Table 1) with less extreme initial densities. We chose $n_{cl} = 4 \times 10^3\,cm^{-3}$, intermediate between two models in the tests, with clumps restricted to the central 75 per cent of the domain in y and z directions and to 45 per cent of the longer x domain. This gave a mass in clumps of $266\,M_\odot$, making up $\simeq$90 per cent of the total gas mass. This was distributed among 40 clumps ranging in mass from 2.4 to $10.4\,M_\odot$ and in radius from 0.06 to 0.14 pc. The peak density in the initial conditions was $n_H \simeq 1.8 \times 10^5\,cm^{-3}$ and the background density was $n_b = 100\,cm^{-3}$. The ionizing source was placed 2 pc off the domain in the long direction and had an ionizing flux of $10^{11}\,cm^{-2}\,s^{-1}$ at the front edge of the grid. This model successfully produced three ET-like structures and we repeated it

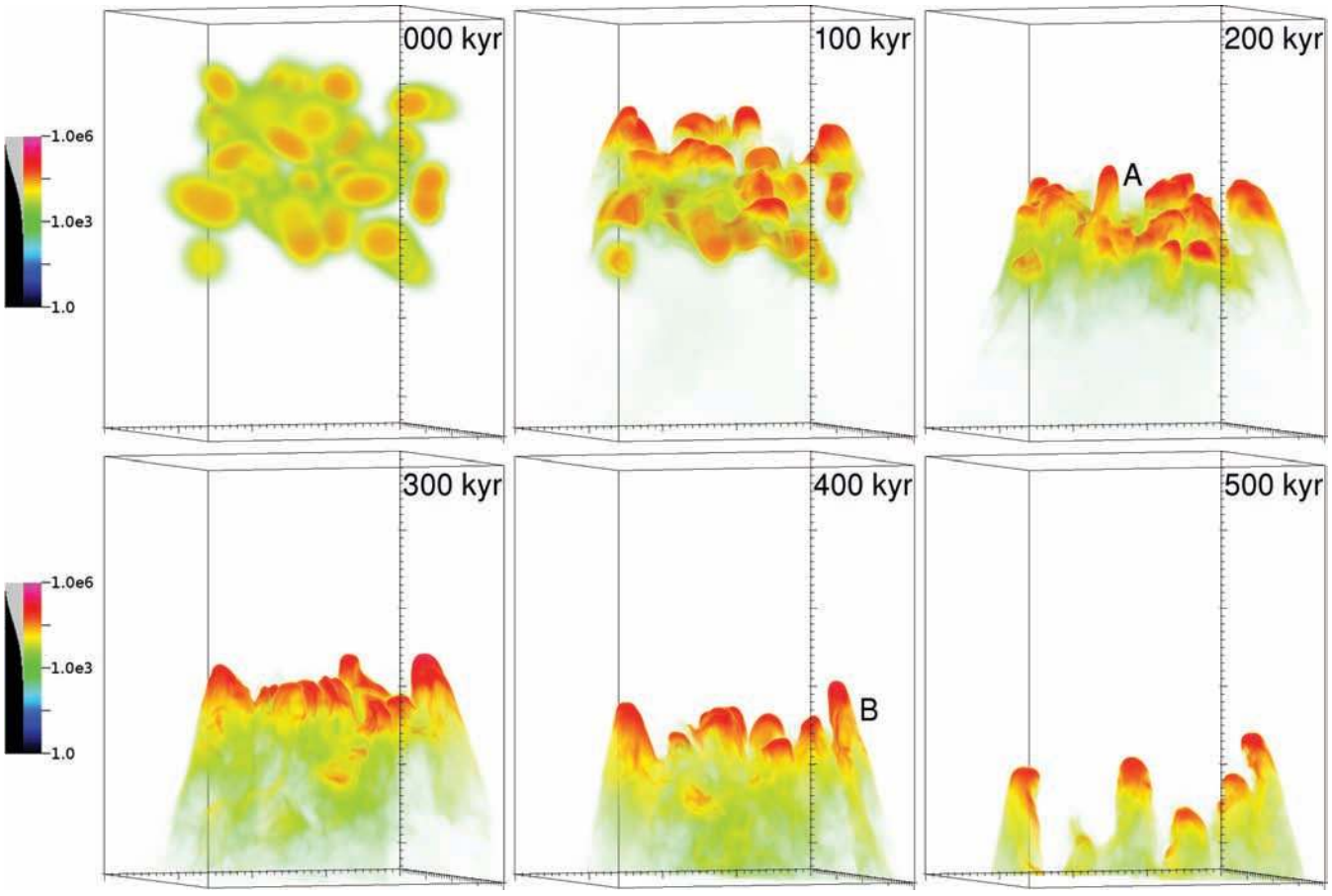

Figure 2. Volume rendering of a 3D simulation of the photoionization of a random clump distribution. Neutral gas density is plotted on a log scale as indicated (in units of cm^{-3}), with gas at $n_\mathrm{H} \lesssim 10^4\,\mathrm{cm}^{-3}$ made transparent to show the difference between neutral tails and dense pillars. Figures are shown for outputs every 100 kyr from 0 to 500 kyr. The source is 2 pc off the top of the domain. Note the pillar labelled 'A' front and centre in the third panel and another labelled 'B' at right back in the later panels.

with 512×384^2 grid cells with a similar physical size of $2.67 \times 2 \times 2\,\mathrm{pc}^3$. A volume rendering of the neutral gas number density is shown in Fig. 2 at 100 kyr intervals from the initial state to 500 kyr. The number density is on a log scale, with gas at $n_\mathrm{H} \lesssim 10^4\,\mathrm{cm}^{-3}$ made transparent (the transfer function is shown beside the log scale). This highlights only the densest structures to distinguish between shadowed regions and dense tails.

After 100 kyr, the front clumps have begun to accelerate away from the source and have clearly been compressed significantly. The first pillar (labelled 'A') forms near the front of the domain after about 170 kyr and lasts for about 50–70 kyr before being accelerated back to the main body of neutral gas. It is about 0.5 pc in length with an aspect ratio of 2–3. This frame also shows a large mass of merged clumps at the far right. By the next frame at 300 kyr, this mass has begun to look more like a pillar, along with another mass at the far left. At 400 kyr both of these structures clearly resemble ETs, with the one on the right (labelled 'B') slightly more developed and measuring about 0.75 pc in length. All neutral gas coloured yellow to red has a number density $n_\mathrm{H} \gtrsim 10^4\,\mathrm{cm}^{-3}$, so these are dense enough to be considered pillars and not just shadows. The pillars are formed almost entirely from dense clump material that has been pushed into the shadowed regions. In the last frame at 500 kyr pillar B has a surprisingly similar morphology to the largest pillar of the three in M16, leaning over its neighbours. This pillar has survived for 200 kyr in the simulation and is likely to live for significantly longer.

We tested the numerical convergence of these results by comparing the structures that formed when this calculation was performed at resolutions of 128^3 and 256^3 (with shorter x domains) with the above simulation. The positions, sizes and lifetimes of the pillars were found to be consistent at all resolutions. Transient peak densities increased with resolution, as expected in problems involving strong compression.

We summarize the basic results from these 3D models as follows. It is easier and more common for a configuration of clumps to produce a structure like a mountain or corrugation than an ET. In particular, in our 3D models we required clumps of a few solar masses in a density field that had substantial low-density regions surrounding the clumps in order to generate ET-like structures. Our best model produced a single short-lived clump after about 170 kyr and two or three longer lived pillars after 300 kyr. No models produced an ET in less than 150 kyr. The pillars we formed were 0.5–0.75 pc long, had number densities of $\gtrsim 10^5\,\mathrm{cm}^{-3}$ at the densest part of the head and of $1\text{–}4 \times 10^4\,\mathrm{cm}^{-3}$ in the denser parts of the trunks. These properties are similar to observed ETs. At 400 kyr, there was $110\,\mathrm{M}_\odot$ of neutral gas in the domain, of which $65\,\mathrm{M}_\odot$ had $n_\mathrm{H} > 10^4\,\mathrm{cm}^{-3}$, divided among two ETs and the other clumps. This gives somewhat lower masses in our ETs than in the M16

pillars (masses of ∼30–90 $M_\odot$), but comparable to estimates for other observed ETs (e.g. Gahm et al. 2006).

4 ANALYSIS OF CLUMP CONFIGURATIONS

Certain configurations of clumps which occurred in the random initial conditions gave rise to pillar-like structures. To investigate how these structures are formed, we have simulated configurations of clumps in isolation to model the formation of pillars A and B. These are models 17 and 18 in Table 1. The calculations used a computational domain with 192×128^2 zones covering 2.25×1.5^2 pc^3, a source at -2 pc in the x direction with a luminosity in ionizing photons of $L_\gamma = 2 \times 10^{50}$ s^{-1} and an ambient gas density of 200 cm^{-3}. We have also run these simulations with 49 small random clumps superimposed on this, corresponding to an extra mean density of 400 cm^{-3}, but found very little difference in the results. Superimposed on this density field are three massive clumps of up to 28.3 $M_\odot$ each, with a peak density of up to $n_H = 10^5$ cm^{-3} (overdensity of 500) and Gaussian profiles with a scale radius of 0.09 pc. We have scaled up the mass and radius of the clumps compared to the previous simulations in order to get closer to the masses and sizes of the M16 pillars, which are ≃30–90 $M_\odot$. As expected for simulations without self-gravity, the results with less massive clumps were very similar except that the time-scales were shorter. In the results that follow, we vary the relative positions of the three clumps. The ionizing flux at the front side of the clumps is about 2.9×10^{11} cm^{-2} s^{-1}. The gas is initially neutral, with constant pressure $p_g/k_B = 2 \times 10^5$ cm^{-3} K, corresponding to 1000 K in the lowest density gas.

4.1 Three almost co-linear clumps (pillar B)

We first investigate the effect of several clumps partially shadowing each other in a roughly linear fashion (model 17), similar to the configuration that formed pillar B. The three massive clumps are located in the same y-plane as the source at positions [0.30, 0.72, 0.72], [0.75, 0.72, 0.84] and [1.2, 0.72, 0.60] (measured in parsecs from a corner of the domain nearest the source). The front clump thus partially shadows the two behind it.

Volume renderings for the run using cooling model C1 are shown in Fig. 3 at times 0, 50, 150 and 250 kyr. At later times, the clumps merge and the structure no longer resembles a pillar. Projections at angles of 20° and 40° to the z-axis (where 0° is perpendicular to the pillar) are shown in Fig. 4, with column density shown in the maps and line-of-sight (LOS) velocity shown in position–velocity (P–V) diagrams below the maps. The 3D P–V data cube is projected on to 2D by summing the contribution of all the pixels in a given image y column at each x position. This means that the normalization of the P–V column densities is on a somewhat arbitrary scale.

Fig. 3 shows how the partially shadowed clumps compress and move sideways into the shadow, while the fully exposed clump is accelerated and merges into them. In this situation the gas is initially aligned as a pillar-like structure, and the compression due to photoionization of the surroundings serves to enhance this appearance for a limited time. The neutral gas only resembles a pillar for 150 kyr; this structure is a relic from the initial conditions as opposed to being generated by dynamical evolution. The P–V diagrams in Fig. 4 clearly show gas moving at very different speeds away from the radiation source, so it is likely that some of this gas will move into the tail as the structure recedes from the source and is subjected to lower ionizing fluxes.

Even though model 16 did not show such a clear early-forming pillar, it is nevertheless interesting that the projected column densities in Fig. 4 show structures that resemble pillars for the first 150 kyr of the simulation. The clumps were not as neatly arranged in the random clumps model, but given that the ISM in molecular clouds tends to be filamentary and clumpy, it is certainly possible that there are some ETs in H II regions which are formed in this way, i.e. purely from initial conditions and not dynamically. This is a less satisfactory explanation for M16, however, since we would need three lines of clumps/filaments positioned beside each other, and all pointing by chance back to the brightest star in the nebula.

Looking at the evolution in more detail, the P–V diagram shows the acceleration of the first clump away from the source, up to about 6 km s^{-1} in 150 kyr (the true velocity is $v_\parallel/\sin\theta$). For all of this time, the shadowed gas remains essentially stationary. The velocity signature of this formation mechanism is very clear, with the head of the pillar receding from the star faster than the trunk. This is the opposite of what is seen in other formation scenarios such as the model of Lefloch & Lazareff (1994) of a tail forming behind a single clump which has the tail streaming away from the star faster than the head. We show the two perspectives at 20° and 40° to demonstrate that even though 20° is close to perpendicular,

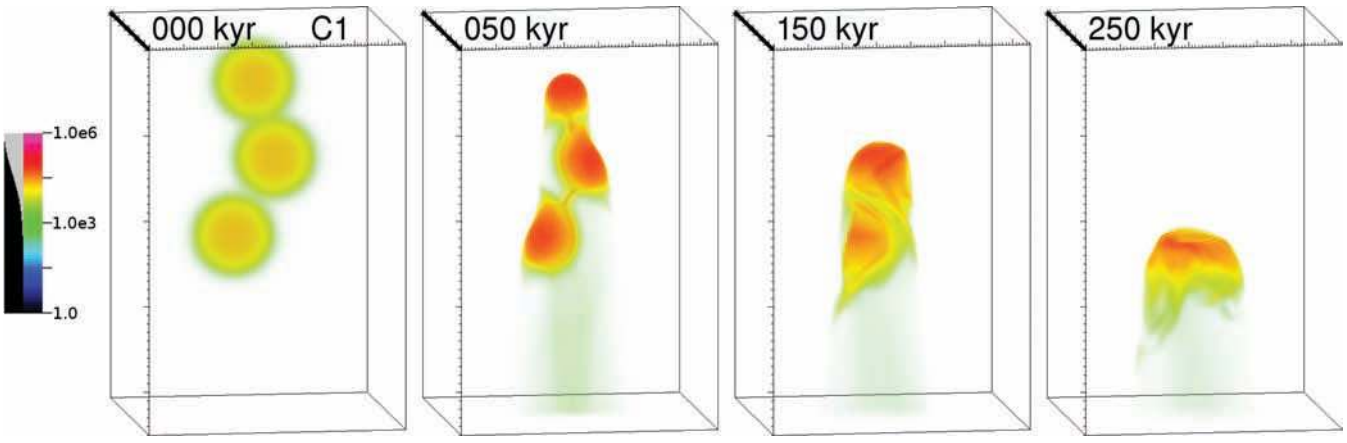

Figure 3. Volume rendering of a 3D simulation of isolated pillar formation with three massive clumps initially almost in a line, using cooling model C1. The neutral gas number density is plotted (cm^{-3}), with low-density gas made transparent to show the difference between low-density neutral tails and dense pillars. The transfer function is shown beside the log scale to the left. Simulation times are indicated on each panel.

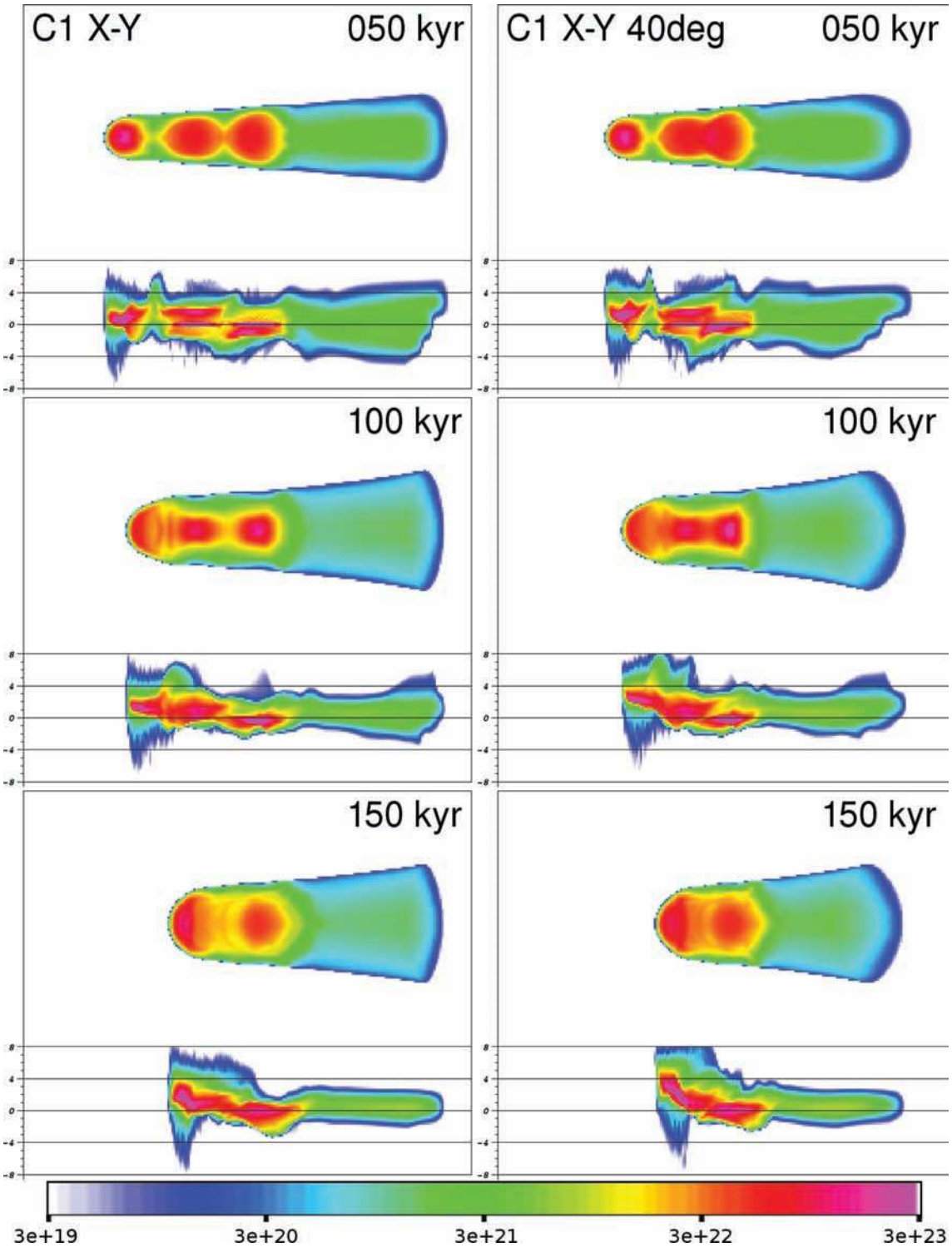

Figure 4. Projections through the 'co-linear clumps' 3D simulation shown in Fig. 3 with cooling model C1. The gas column density of neutral (atomic) hydrogen is plotted in a 2D projection above and a position–velocity diagram below (with radial velocities indicated in units of km s^{-1}). Times are indicated on each panel. The normal vector for the projections is at angles of 20° and 40° from the z-axis in the left and right sequences, respectively, and is perpendicular to the y-axis. The column density is shown on a log scale as indicated (in units of cm^{-2}).

they both show the same trends in velocity along the pillar (in subsequent figures, we only show 20° projections).

We note, however, that the almost linear decrease in LOS velocity from the head to the tail is significantly enhanced by transverse motions in the gas. The middle clump is being pushed away from the observer into the shadow and the rightmost clump towards us (cf. Fig. 3). If we make the same projections from the opposite side of the simulation, these transverse velocities are reversed leading to

a much less obvious velocity gradient (although the large velocity at the head is still evident). We return to this issue in Section 5 where we show velocity profiles from different perspectives.

4.2 Triangle of three clumps (pillar A)

We now investigate a more dynamical situation (model 18) in which two clumps are pushed past a third which was initially shadowed, and are wrapped around into the tail, forming a pillar. This was how the short-lived 'pillar A' formed in model 16, and it also crudely models the later evolution of pillar B. In this scenario, the three massive clumps are placed at positions [0.45, 0.72, 0.6], [0.45, 0.72, 0.9] and [0.75, 0.72, 0.72], giving us two clumps in front shadowing the third clump, all in the plane $y = 0.72$ pc. This plane also contains the source at [−2.0, 0.72, 0.72]. The properties of the two front clumps were modified to have masses $M = 27.7\,\mathrm{M}_{\odot}$, peak overdensities of 250 and scale radii of 0.1125 pc, while the shadowed clump has a mass of $M = 28.3\,\mathrm{M}_{\odot}$, overdensity of 500 and scale radius of 0.09 pc, as in the previous model. The formation of a pillar in this configuration is quite sensitive to the relative clump positions; if the front clumps are too close together or too dense they do not move past the shadowed one without disrupting it and if they are too far apart they never merge with the shadowed clump to form a single clump/pillar configuration.

We first ran this simulation using cooling model C1, and a volume rendering of the results is shown in Fig. 5. The pillar develops more slowly than in the previous scenario, taking around 200–250 kyr to form, because the gas has to travel further to get into the tail. Initially the front two clumps are compressed and slowly accelerated, seen after 50 kyr in Fig. 5. They collide obliquely with the shadowed third clump, which then starts to accelerate due to a combination of being exposed to ionizing radiation and to the shocks driven through it by the passage of the first two clumps. Material from the remains of the first two clumps sweeps into the tail region after 200 kyr, producing the pillar-like structure seen in the last panel at 250 kyr. In this model the ET structure is formed dynamically rather than being left over from initial conditions, and the column of neutral gas resembles a pillar only after 250 kyr, unlike the previous model.

As one might expect from the initial conditions, this column is quite asymmetric; it is much broader in one direction than the other at late times. The volume rendering shows it from the narrower perspective; projections at 20° from perpendicular to the pillar are shown in Fig. 6 with edge-on projections at right and face-on at left. The gas in the trunk is at volume densities of 1–3 × 10^4 cm^{-3}, but projecting through the narrow axis does not build up enough column density to resemble a pillar whereas the projection through the broad axis clearly resembles an ET at 250 kyr.

The velocity profiles show a broad range of velocities which vary significantly with perspective and over the evolution of the system. We do not see a strong signature here as was seen in Fig. 4. One interesting feature is seen in the right *P–V* diagram at 150 kyr. This shows high velocity gas from the two front clumps which has pushed past the third and moved into the trunk away from the head. This is a similar profile to that of Lefloch & Lazareff (1994) for gas streaming from the head into the tail of a cometary globule. The feature is not clearly seen in the left-hand panel because the tail is strongly re-expanding along the LOS, leading to a broad velocity profile which has the opposite slope from head to tail compared to the right-hand panel. Here, transverse motions are once again masking the true trend in recession velocity from the star along the pillar.

5 EFFECT OF COOLING ON PILLAR FORMATION

Mellema et al. (2006a) use a cooling model similar to our C1 model, with relatively little neutral gas cooling, to model the global expansion of an H II region into a turbulent density field. Individual features are not highly resolved, but it is clear that their results (e.g. their fig. 5) are qualitatively similar to ours, showing fairly smooth coherent pillar-like structures. In particular, both they and we do not find I-front instabilities developing or any fragmentation which is a feature of simulations with strong neutral cooling. This is undoubtedly due to the thermal physics, since it has been shown by Williams (2002) and Whalen & Norman (2008), among others, that instabilities in D-type I-fronts are strongest when the neutral gas can cool rapidly. These instabilities can generate dense finger-like structures (e.g. Mizuta et al. 2006; Whalen & Norman 2008) but it is unclear if they could generate something as massive and large as the M16 complex of pillars.

Other authors (e.g. Lefloch & Lazareff 1994; Williams et al. 2001; Gritschneder et al. 2009; Lora et al. 2009) have used a thermal model where the neutral gas is cold and isothermal, leading to strong fragmentation and instability in the I-front. Observationally, White

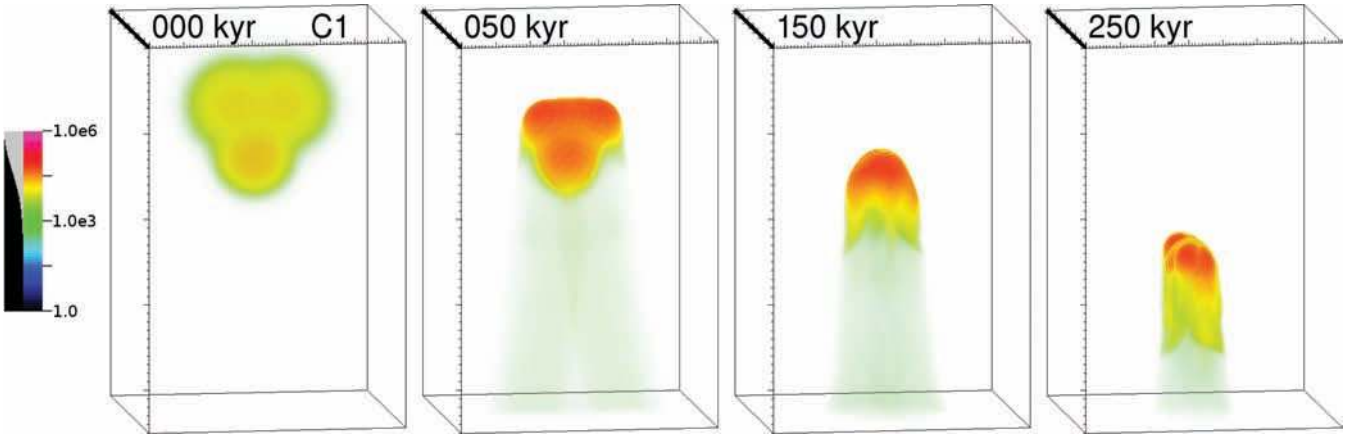

Figure 5. Volume rendering of a 3D simulation of isolated pillar formation with three massive clumps initially in a triangle configuration, using cooling model C1. The neutral gas number density is plotted (cm^{-3}), with low-density gas made transparent to show the difference between low-density neutral tails and dense pillars.

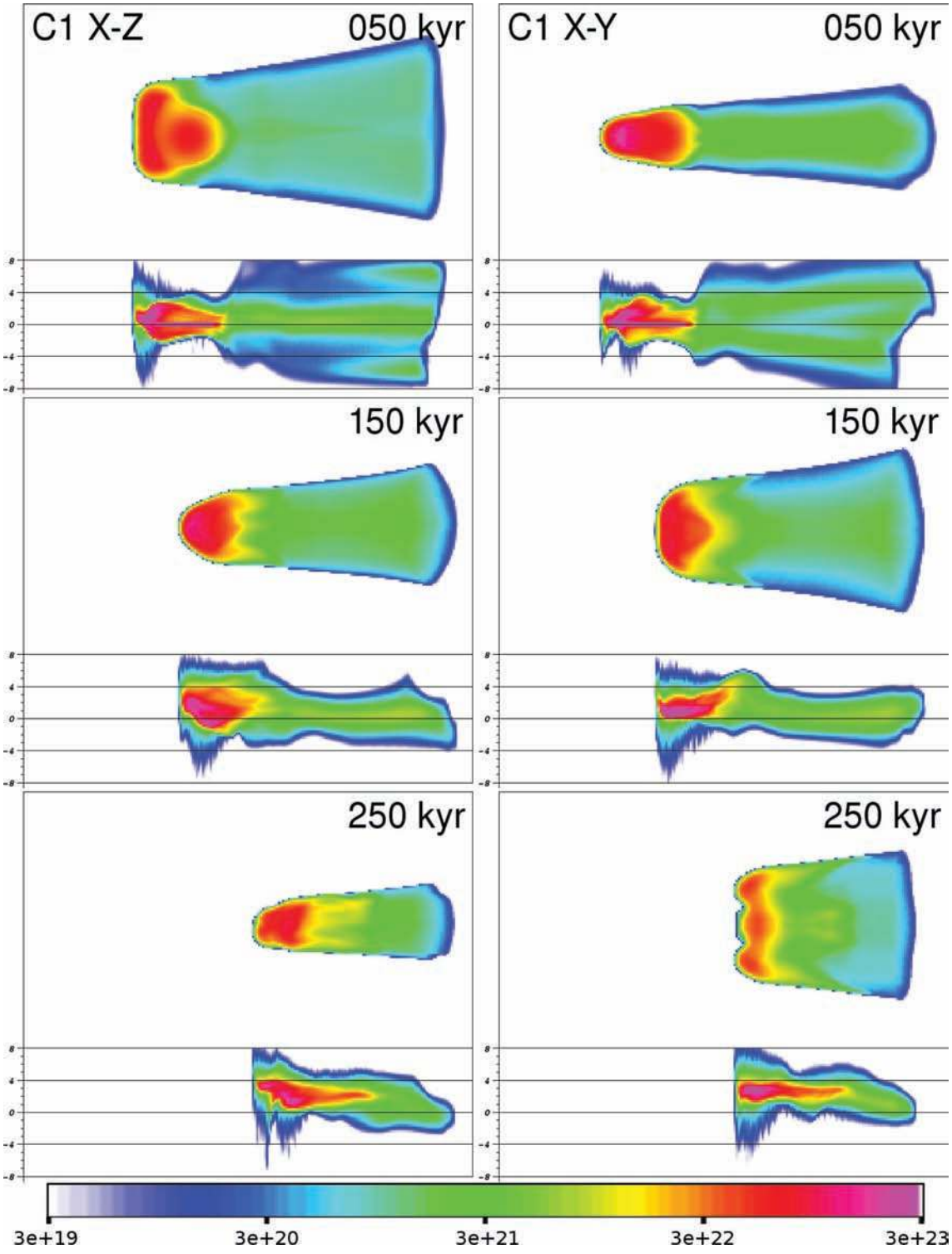

Figure 6. Projections through the 'triangle of clumps' 3D simulation shown in Fig. 5 with the C1 cooling model. The projection is at 20° to the *y*-axis on the left and to the *z*-axis on the right. The two front clumps are projected on to each other in the right sequence of figures.

et al. (1999) showed that the M16 pillars have cold cores ($T \sim$ 10–20 K), warm trunks or fingers ($T \sim 60$ K), and a 'hot' shell of surrounding gas at $T \sim 250$–320 K. To study the possible effects of these temperature variations, Miao et al. (2006) use a much more detailed thermal model to study the head of a pillar numerically, but at the expense of using very low resolution for the dynamics. More recently, Henney et al. (2009) have fitted a number of functions to detailed calculations of cooling and heating rates for their MHD models of photoevaporating clumps. They found that the shadowed neutral gas was not isothermal, but had a range of temperatures comparable to observed values. These results show that while the isothermal approximation is expected to be more realistic than our C1 model, it is unclear whether it is sufficient to capture the details of ET formation.

To investigate the influence neutral gas cooling has on our results, we have repeated the simulations in the previous section using cooling model C2, designed to be intermediate between C1 and the isothermal approximation. In comparison to Henney et al. (2009), their 'molecular' cooling rate (which they denote $L_{\rm PDR}$) scales as $L \propto \rho^{1.6}\,{\rm erg\,cm^{-3}\,s^{-1}}$ whereas our C2 model scales as $L \propto \rho$. So while our model has significant neutral gas cooling down to 100 K, very dense gas cools more rapidly in their simulations, closer to an isothermal model.

Volume rendering of the linear and triangular clump configurations with C2 cooling is shown in Figs 7 and 8, respectively. The evolution is slower than with C1, so we show the results at times of 50, 150, 250 and 350 kyr on the same neutral gas number density scale. Comparing the 50 kyr panels between the C1 and C2 runs, the main change is immediately apparent. The extra neutral gas cooling makes shocks more compressive and slower moving. This can be clearly seen in the shadowed region, where the converging shock is about 10× denser in Fig. 7 than in Fig. 3. The cooling also affects the exposed clump; the radiatively driven implosion phase is slower and the clump is compressed to a greater degree. The rocket effect is less effective on this exposed clump: first, there is a smaller surface area to absorb the photon flux; secondly, the denser gas in the I-front and in the photoevaporation flow leads to faster recombinations and thus more photons are required to ionize an atom and keep it ionized until it flows away from the I-front.

Comparing the 150 and 250 kyr panels of Figs 3 and 7, the difference is dramatic. The leading clump has fully merged into the second in the C1 run, and the implosion phase is followed by a strong re-expansion. Re-expansion in the C2 run is much weaker because most of the heat generated is radiated away before it can instigate a rebound. We obtain a much narrower and denser structure which resembles an ET for at least 200 kyr. The initial configuration is enhanced rather than disrupted by the photoionization process.

Fig. 8 shows a very similar story for the triangle of clumps. The system's evolution is slower, the shocks are more compressive and there is less re-expansion after the implosion phase. The general picture from these two models is that ETs are longer, narrower, denser, longer lived and have more substructure with the C2 cooling prescription. While qualitatively the same evolutionary scenario plays out, quantitatively the neutral gas cooling has a significant effect on the results.

Projections through the C2 runs are shown in Figs 9 and 10. Fig. 9 shows the projection at 20° as in the left sequence of Fig. 4 for C1, but the two sequences show projections from the front and rear perspectives. The column density maps are similar from both perspectives, and it is clear that the structure resembles an ET at all times shown. The left *P*–*V* diagrams show the same trend as in the C1 model, where gas at the head is receding more rapidly from the star than the trunk is, but this trend takes significantly longer to become established. The right-hand *P*–*V* diagrams also show the

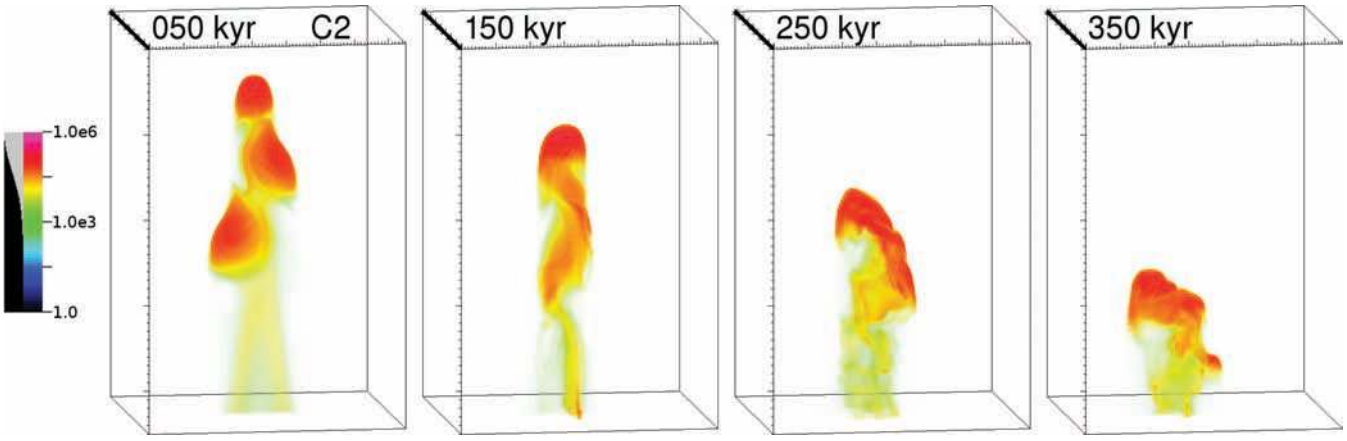

Figure 7. As Fig. 3, but with the simulation run with cooling model C2. Simulation times are indicated on each panel.

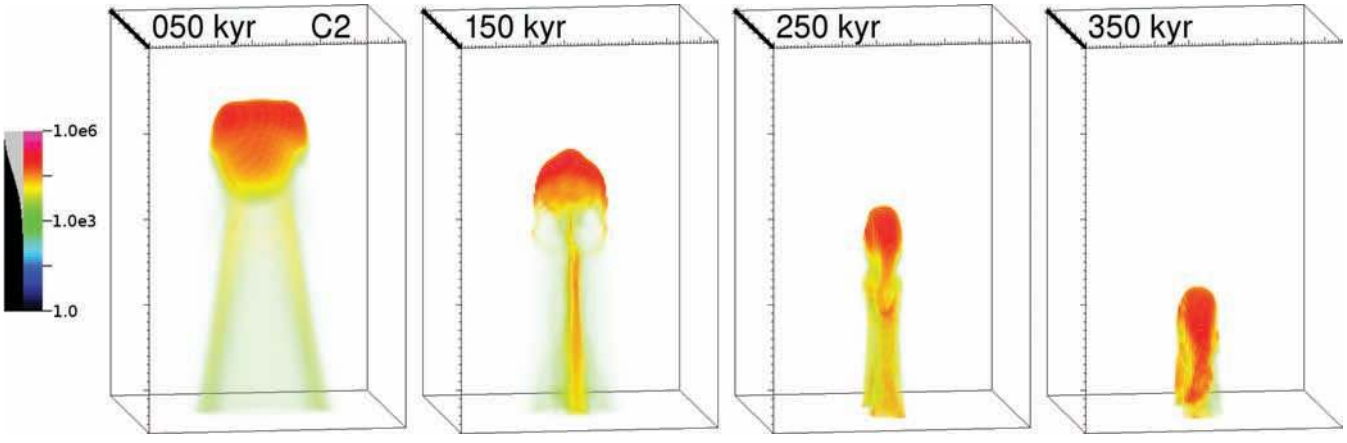

Figure 8. As Fig. 5, but with the simulation run with cooling model C2 and with frames at different times.

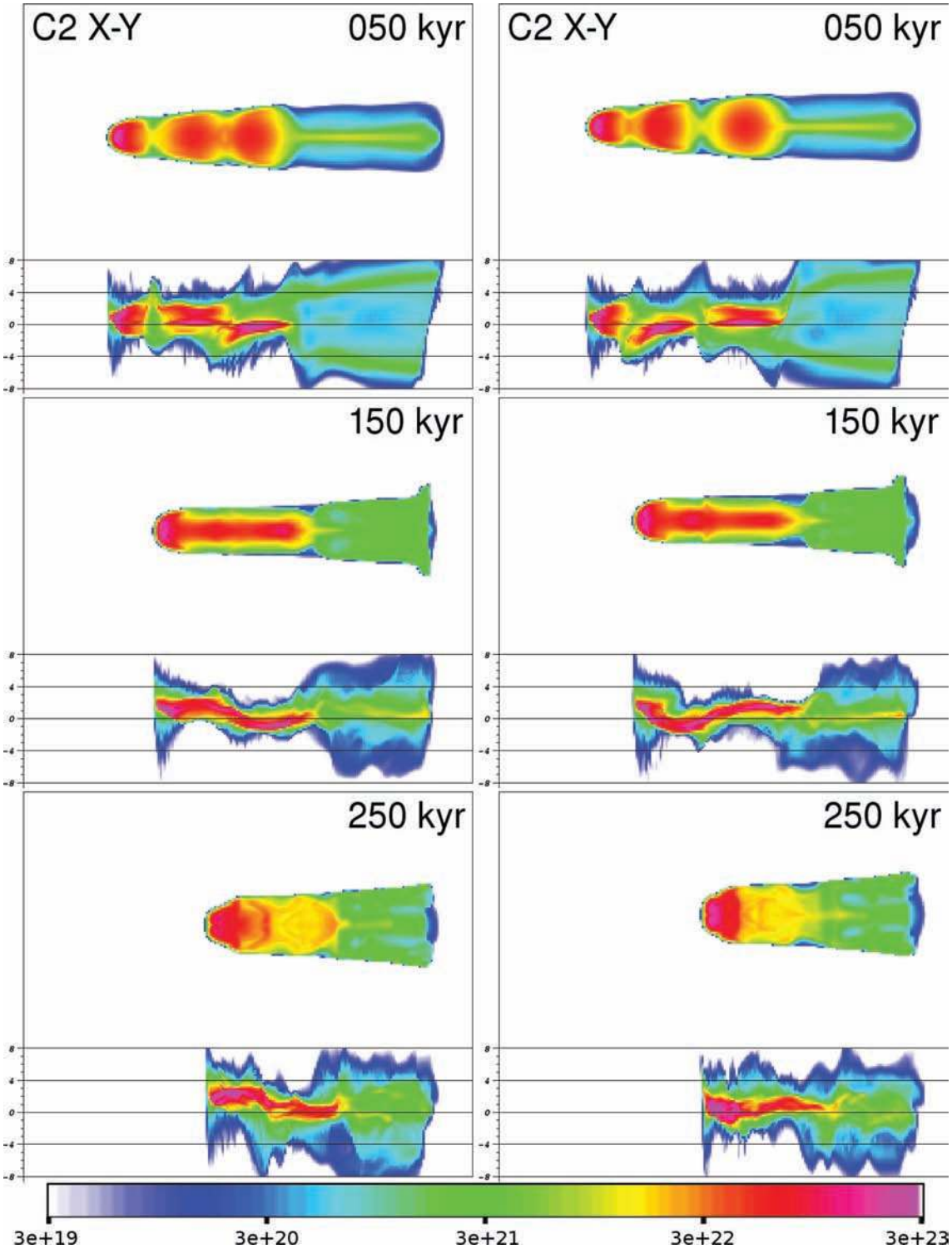

Figure 9. Projections through the 'co-linear clumps' 3D simulation shown in Fig. 7 with cooling model C2. Only the projection at 20° to the z-axis is shown, but from the front of the domain at left and from the rear at right. This highlights the effect transverse gas motions can have on velocity profiles.

head receding rapidly, but the gas from the partially shadowed clumps has very different LOS velocities due to transverse motions. This particular case shows how difficult it is to infer anything about a formation scenario from a *P*–*V* diagram. With non-axisymmetric initial conditions, transverse motions mix with the recession velocity in an unpredictable way and are a strong contaminant when one wants to measure the recession velocity along the length of a pillar.

Fig. 10 shows projections face-on and edge-on through the triangle of clumps scenario, again at 20° to perpendicular. The same asymmetry as shown in Fig. 6 is apparent, but to a lesser degree, and the C2 run shows that the column of gas resembles an ET in both directions from 200 to 300 kyr, albeit much more convincingly in the left-hand sequence. The *P*–*V* diagrams show very little trend in velocity along the length of the pillar at most times, but again it can

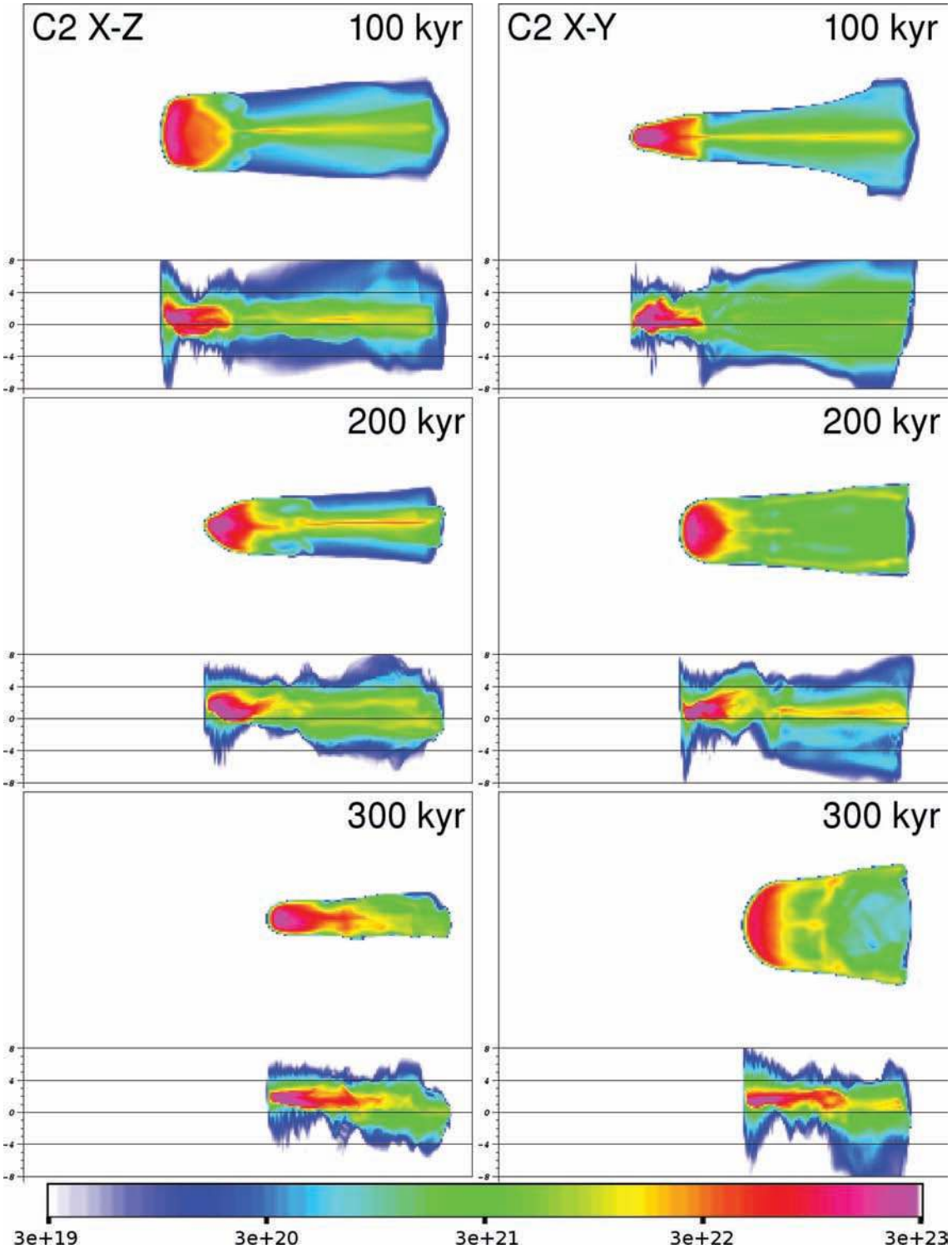

Figure 10. Projections through the 'triangle of clumps' 3D simulation shown in Fig. 8 with the C2 cooling model. The projections are at 20° to the *y*-axis on the left and to the *z*-axis on the right, as in Fig. 6 but shown at different times to reflect the slower evolution of this model.

be seen in the 200 kyr panels that there is high velocity gas moving from the head into the tail region, as was seen in the C1 model.

6 DISCUSSION

Williams et al. (2001) performed axisymmetric simulations with a similar aim to our work – to investigate the mechanisms by which ETs can form. They modelled parallel rays rather than treating the radiation from a source at a finite distance. In most of their models, Williams et al. (2001) start with a dense ($n \sim 10^4\,\mathrm{cm}^{-3}$) layer of gas at the boundary most distant from the star. This served both to stall the I-front and to provide a reservoir of dense gas from which to build up a pillar. This is a very similar picture to that modelled more recently in 3D by Raga et al. (2009), who studied small

($l \sim 0.03$ pc) columns of dense gas forming in a photoionized region. Their initial conditions had an effectively infinite reservoir of neutral gas shadowed by smaller clumps. Evaporating gas from the reservoir flowed into the shadowed regions forming dense columns as it recombined and cooled. These authors have demonstrated a mechanism by which ETs can form given a sufficiently large reservoir of dense gas behind a shadowing clump. We consider alternate scenarios, however, where the ET must be built up from clumps of comparable mass and from low-density interclump gas. We find that this is sufficient to produce pillars when the gas is in certain configurations, but we also find that they do not form as readily as found by Williams et al. (2001). This is quite important: while ETs are seen in many H II regions, structures resembling heaps and corrugations which are not elongated are much more common. The mechanisms by which ETs form cannot therefore be too efficient or many more ETs would be observed.

The fact that most H II regions seem to have one or two ET structures led Williams et al. (2001) to suggest that they may be long-lived objects, with lifetimes comparable to the H II region, a proposition supported by their simulation results. An alternative scenario is that they are short lived (∼100 kyr), but multiple generations of them occur during the expansion of an H II region. For models where the gas is not already organized in a linear structure, we do not find any pillars forming in less than 150 kyr. Adding extra cooling in the neutral gas only lengthens this formation time. Additionally, it takes about 250–300 kyr before more massive and long-lived pillars start to form dynamically. This is the rough timescale for dense neutral gas to be accelerated, pushed past other dense clumps and stretched out into a long tail. We suggest that it would be difficult to dynamically generate a parsec-scale dense ET from static initial conditions in less than 150 kyr, and our results are consistent with the claim by Williams et al. (2001) that ETs are likely to be long-lived structures.

6.1 Gas pressure

Observational age constraints are thus far not very stringent. An upper age limit for ETs is set by the age of their H II region. The free-fall time of the densest parts of the pillars does not constrain their age as the gas is being actively compressed and so the free-fall time is changing as the structures evolve. If the pressure difference between the neutral and ionized gas is very large, however, this may indicate that the dense gas has not had time to dynamically respond to the photoionization, and so the structures must be young, perhaps younger than their sound crossing time. In M16, the gas pressure at the base of the ionized photoevaporation flow has been estimated by Hester et al. (1996) to be $p_g/k_B = 6 \times 10^7$ cm^{-3} K. The internal pressure in the densest parts of the pillars was estimated by White et al. (1999) to be $p_g/k_B = 3.5 \times 10^7$ cm^{-3} K. These values are based on temperature and density estimates in ionized and neutral gas, respectively. White et al. (1999) interpreted this pressure difference as suggesting that the ETs in M16 may be young, with the dense clumps currently undergoing the early stages of radiation-driven implosion (Bertoldi 1989). In our simulations the peak pressure at the I-front varies between $p_g/k_B = 5 \times 10^7$ and 2×10^8 cm^{-3} K, and in the neutral ETs between $p_g/k_B = 2 \times 10^6$ and 5×10^7 cm^{-3} K. These values are consistent with the observations, but we found that an equilibrium state was never reached in our models. The pressure varies by large factors both in time and in space along the length of the ET, and the peak pressure changes in time according to the instantaneous density at the I-front. These results suggest that the observed pressure difference (a factor of 1.7) should not be taken as strong evidence that the pillars are young since we find pressure variations much larger than this within the dense neutral gas. A caveat to this is that our thermal modelling of the neutral gas is crude and gas pressure is sensitive to this, so it would require more detailed modelling to make a definitive statement. We can say that simulations with both cooling models C1 and C2 have these pressure variations, and we believe that the dynamical nature of the ETs which form in our models will always generate significant pressure gradients within the ETs. It would be interesting to compare this with structures formed via I-front instabilities to see how their internal dynamics differ.

6.2 Morphology of ETs

Molecular emission traces the projected mass density of ETs and has shown them to be rather more clumpy than they appear in optical data (Pound 1998; White et al. 1999), with significant density variations along their length. The heads of the pillars are the densest regions, with clumpy lower density gas found in the trunk. Our simulations support this clumpy model for the underlying density structure; in some of our models, the clumps maintain their identity for hundreds of kyr (e.g. Fig. 9). We also find that the highest density gas is always found in the head of the pillars because the strongest compression is always found ahead of the I-front which drives the dynamics. We have also calculated optical emission maps due to recombination radiation (e.g. Hα) in the manner described by Henney, Arthur & García-Díaz (2005), using a constant dust opacity as in Mellema et al. (2006a). An image from the co-linear clumps' simulation (model 17) at 250 kyr is shown in Fig. 11; this can be compared to the bottom left-hand panel of Fig. 9 which shows projected neutral gas density and is closer to what we expect from a molecular emission map. It is clear that the 'optical' image shows a much smoother structure which appears more like the *HST* images of M16. In particular, the dense parts of the pillar's trunk are completely dark in the optical image while there is substructure in the projected density. Our image has less substructure than the *HST* images; this is likely due to the limited spatial resolution of our simulations and possibly because our cooling models do not promote the development of I-front instabilities.

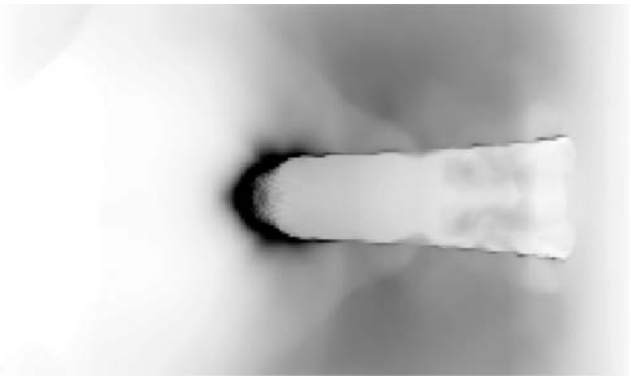

Figure 11. Simulated Hα emission map from our simulation of a pillar forming from three almost co-linear clumps using cooling model C2. The map can be compared to projected density in the bottom left-hand panel of Fig. 9. The scale used is linear with the strongest emission in black and deliberately saturated to bring out low contrast features.

6.3 Position–velocity diagrams

The full 3D nature of our simulations has allowed us to calculate LOS velocity profiles through the ETs which include asymmetric transverse motions. We have shown that these motions can largely determine the observed profile (Fig. 9). This has implications for interpreting the *P–V* diagrams in Pound (1998) and White et al. (1999), in particular for the largest M16 pillar which has a velocity gradient that changes sign from the head to the tail. This was interpreted as evidence that the head and tail are separate structures, but this is difficult to reconcile with optical observations. Our results suggest a resolution to this apparent contradiction: this pillar could have started out as two separate dense clumps which have since merged but have kept their identity in velocity space. Fig. 9 shows just such a case where the clumps gain opposing transverse velocities, giving the projected velocity profile an S-shape which is maintained for >100 kyr despite the clumps having merged into a pillar much earlier.

For the smallest of the M16 pillars, Pound (1998) notes that the shadowing implies that it is closer to us than the ionizing stars so we expect the tail to stream towards us faster than the head. In fact, the opposite is true. Our results also offer two possible explanations for these observations: (i) it could be due to a strong transverse motion in the pillar if it is seen close to edge-on or (ii) it could be formed from a column of dense gas closely aligned with the radiation propagation direction. Our models of this situation show that for at least some of the pillar's evolution, the head can be receding from the star faster than the tail.

6.4 Influence of other physical processes

We have already discussed in detail the effects of neutral gas cooling on our results, but there are a number of other processes which could contribute significantly. Since massive stars generate strong winds, Raga, Steffen & González (2005) studied photoevaporating clumps interacting with a stellar wind, finding that when the photoionization was sufficiently intense the photoevaporation flow effectively shielded the clumps from the wind. This gives us confidence that ionizing radiation is the main driver of ET formation. Raga et al. (2009) studied photoionization models with a basic treatment of diffuse radiation. They found that there was no strong difference between runs with the diffuse radiation and runs where they used the on-the-spot approximation. This suggests that, while diffuse radiation would undoubtedly change our results somewhat, it is unlikely to make a dramatic difference. Esquivel & Raga (2007) studied the effects of self-gravity on the photoionization of a dense cloud of gas using a two-temperature equation of state (i.e. the neutral gas is isothermal), which gives rise to strong instabilities and fragmentation associated with the photoionization process. Interestingly, they found that self-gravity had little effect on the overall process of the evaporation and fragmentation of the massive clump, and was only significant in determining the properties of the densest sub-clumps produced by the fragmentation. This supports our implicit assertion in this work that pressure forces are the dominant driver in the evolution of photoevaporating clumps, at least in the early stages.

7 CONCLUSIONS

Using moderately high-resolution 3D radiation-hydrodynamics simulations of clumpy density fields exposed to ionizing radiation from a point source, we have investigated how effectively shadowing can generate pillar-like structures. We have shown that even in the absence of self-gravity or I-front instabilities, large parsec-scale ETs can form dynamically solely due to this shadowing.

Of our 2D and 3D models, about 20 per cent produced long-lived pillars. This is more due to our choices of initial conditions than how easy or difficult it is to generate ETs. Nevertheless, we did find certain density fields more conducive than others to forming pillars. The most successful of these contain both large low-density regions where the I-front can propagate far from the source, and also massive clumps with sufficiently high density and inertia to stall the I-front for >100 kyr. Pillars are formed with diameters comparable to those of the clumps that give rise to them.

Simulations of specific configurations of massive clumps show that pillar-like initial conditions evolve with a different velocity signature to configurations where the ETs form dynamically from clumps that are not initially co-linear. For a simulation with three clumps initially almost co-linear, we find that the head of the ET recedes from the source more rapidly than the shadowed trunk which has not been exposed to radiation. For dynamically forming ETs, gas streams into the shadowed trunk past the head and is thus moving faster than, or at a comparable speed to, the pillar's head. This could produce a noticeable observational signature from which these two formation mechanisms can be distinguished, but we find that the *P–V* diagrams vary significantly with viewing angle due to transverse gas motions. This variation increases with the degree of asymmetry and the transverse motions significantly contaminate attempts to measure recession velocity in the pillars. These transverse motions offer an explanation for the features seen in *P–V* diagrams for the pillars in M16.

We have shown that neutral gas cooling has a very strong influence on the modelling results. Stronger cooling produces ETs which take longer to form dynamically, are narrower and denser, and are more resistant to the rocket effect and hence live longer. This shows that the complex chemistry and thermal physics in molecular clouds may play a crucial role in ET formation and evolution. For the specific case of almost co-linear clumps, the initial pillar-like configuration was slowly disrupted in simulations with the C1 cooling model. By contrast it was enhanced with the C2 cooling model, also proving to be long-lived.

We have not addressed magnetic fields in this work. Henney et al. (2009) have studied the photoionization of a magnetized globule, finding that strong uniform fields can have a significant influence on the evolution of the photoionization process. In future work we will investigate the effects of more realistic thermal physics, as well as the presence of magnetic fields, on the results we have presented here.

ACKNOWLEDGMENTS

JM is funded by the Irish Research Council for Science, Engineering and Technology, funded by the National Development Plan. AJL is funded by a Schrödinger Fellowship from the Dublin Institute for Advanced Studies. Figures were generated using the *VisIt* visualization tool. The authors wish to acknowledge the SFI/HEA Irish Centre for High-End Computing (ICHEC) for the provision of computational facilities and support, and are grateful to Turlough Downes and Garrelt Mellema for suggestions which improved the presentation of this work. They thank the referee for very helpful comments which significantly improved the paper.

REFERENCES

Agertz O. et al., 2007, MNRAS, 380, 963
Bertoldi F., 1989, ApJ, 346, 735
Bertoldi F., McKee C. F., 1990, ApJ, 354, 529
Brandner W. et al., 2000, AJ, 119, 292
Carlqvist P., Gahm G. F., Kirsten H., 2003, A&A, 403, 399
Esquivel A., Raga A. C., 2007, MNRAS, 377, 383
Falle S. A. E. G., Komissarov S. S., Joarder P., 1998, MNRAS, 297, 265
Frieman E. A., 1954, ApJ, 120, 18
Gahm G. F., Carlqvist P., Johansson L. E. B., Nikolić S., 2006, A&A, 454, 201
Gritschneder M., Naab T., Walch S., Burkert A., Heitsch F., 2009, ApJ, 694, L26
Henney W. J., Arthur S. J., García-Díaz M. T., 2005, ApJ, 627, 813
Henney W. J., Arthur S. J., De Colle F., Mellema G., 2009, MNRAS, 398, 157
Hester J. J. et al., 1996, AJ, 111, 2349
Hummer D. G., 1994, MNRAS, 268, 109
Innes D. E., Giddings J. R., Falle S. A. E. G., 1987, MNRAS, 226, 67
Kahn F. D., 1958, Rev. Modern Phys., 30, 1058
Lefloch B., Lazareff B., 1994, A&A, 289, 559
Lim A. J., Mellema G., 2003, A&A, 405, 189
Lora V., Raga A. C., Esquivel A., 2009, A&A, 503, 477
Mac Low M.-M., Toraskar J., Oishi J. S., Abel T., 2007, ApJ, 668, 980
Mellema G., Arthur S. J., Henney W. J., Iliev I. T., Shapiro P., 2006a, ApJ, 647, 397
Mellema G., Iliev I. T., Alvarez M. A., Shapiro P. R., 2006b, New Astron., 11, 374
Miao J., White G. J., Nelson R., Thompson M., Morgan L., 2006, MNRAS, 369, 143
Mizuta A., Kane J. O., Pound M. W., Remington B. A., Ryutov D. D., Takabe H., 2006, ApJ, 647, 1151
O'Dell C. R., Handron K. D., 1996, AJ, 111, 1630
Osterbrock D. E., 1989, Astrophysics of Gaseous Nebulae and Active Galactic Nuclei. University Science Books, Mill Valley, CA
Pound M. W., 1998, ApJ, 493, L113
Pound M. W., Kane J. O., Ryutov D. D., Remington B. A., Mizuta A., 2007, Ap&SS, 307, 187
Press W. H., Teukolsky S. A., Vetterling W. T., Flannery B. P., 1992, Numerical Recipes in C: The Art of Scientific Computing, 2nd edn. Cambridge Univ. Press, Cambridge
Quirk J. J., 1994, Int. J. Numer. Methods Fluids, 18, 555
Raga A. C., Mellema G., Arthur S. J., Binette L., Ferruit P., Steffen W., 1999, Rev. Mex. Astron. Astrofis., 35, 123
Raga A. C., Steffen W., González R. F., 2005, Rev. Mex. Astron. Astrofis., 41, 45
Raga A. C., Henney W., Vasconcelos J., Cerqueira A., Esquivel A., Rodríguez-González A., 2009, MNRAS, 392, 964
Raymond J. C., 1979, ApJS, 39, 1
Reach W. T. et al., 2004, ApJS, 154, 385
Stone J. M., Gardiner T. A., Teuben P., Hawley J. F., Simon J. B., 2008, ApJS, 178, 137
Sutherland R. S., Dopita M. A., 1993, ApJS, 88, 253
Toro E. F., 1999, Riemann Solvers and Numerical Methods for Fluid Dynamics. Springer-Verlag, Berlin
Voronov G. S., 1997, Atomic Data Nuclear Data Tables, 65, 1
Whalen D. J., Norman M. L., 2008, ApJ, 672, 287
White G. J. et al., 1999, A&A, 342, 233
Williams R. J. R., 2002, MNRAS, 331, 693
Williams R. J. R., Ward-Thompson D., Whitworth A. P., 2001, MNRAS, 327, 788
Woodward P. R., Colella P., 1984, J. Chemical Phys., 54, 115

This paper has been typeset from a TEX/LATEX file prepared by the author.